Comprehensive high-precision highaccuracy equation of state and coexistence properties for classical Lennard-Jones crystals and low-temperature fluid phases ©

Cite as: J. Chem. Phys. **149**, 204508 (2018); https://doi.org/10.1063/1.5053714 Submitted: 24 August 2018 . Accepted: 25 October 2018 . Published Online: 30 November 2018

Andrew J. Schultz, and David A. Kofke 🗓

COLLECTIONS



This paper was selected as an Editor's Pick







ARTICLES YOU MAY BE INTERESTED IN

Perspective: Excess-entropy scaling

The Journal of Chemical Physics 149, 210901 (2018); https://doi.org/10.1063/1.5055064

The Stokes-Einstein relation for simple fluids: From hard-sphere to Lennard-Jones via WCA potentials

The Journal of Chemical Physics 149, 214501 (2018); https://doi.org/10.1063/1.5054577

Perspective: Computational chemistry software and its advancement as illustrated through three grand challenge cases for molecular science

The Journal of Chemical Physics 149, 180901 (2018); https://doi.org/10.1063/1.5052551

The Journal of Chemical Physics

Submit Today



The Emerging Investigators Special Collection and Awards Recognizing the excellent work of early career researchers!



Comprehensive high-precision high-accuracy equation of state and coexistence properties for classical Lennard-Jones crystals and low-temperature fluid phases

Andrew J. Schultz and David A. Kofke

Department of Chemical and Biological Engineering, University at Buffalo, The State University of New York, Buffalo, New York 14260-4200, USA

(Received 24 August 2018; accepted 25 October 2018; published online 30 November 2018)

We report equilibrium molecular simulation data for the classical Lennard-Jones (LJ) model, covering all thermodynamic states where the crystal is stable, as well as fluid states near coexistence with the crystal; both fcc and hcp polymorphs are considered. These data are used to compute coexistence lines and triple points for equilibrium among the fcc, hcp, and fluid phases. All results are obtained with very high accuracy and precision such that coexistence conditions are obtained with one to two significant figures more than previously reported. All properties are computed in the limit of an infinite cutoff radius of the LJ potential and in the limit of an infinite number of atoms; furthermore, the effect of vacancy defects on the free energy of the crystals is included. Data are fit to a semi-empirical equation of state to within their estimated precision, and convenient formulas for the thermodynamic and coexistence properties are provided. Of particular interest is the liquid-vapor-fcc triple point temperature, which we compute to be $0.694\,55\pm0.000\,02$ (in LJ units). *Published by AIP Publishing*. https://doi.org/10.1063/1.5053714

I. INTRODUCTION

The Lennard-Jones (LJ) model is a single-site pair potential that has been used for decades as a basis for understanding the thermophysical behavior of simple fluids and solids. Its form captures the key effects of interatomic repulsion and attraction, and it is employed as a component in many empirical force fields. The model is specified by a spherically symmetric pairwise-additive energy $u^{(2)}$ as a function of separation r,

$$u^{(2)}(r) = 4\epsilon \left[\left(\frac{\sigma}{r} \right)^{12} - \left(\frac{\sigma}{r} \right)^{6} \right]. \tag{1}$$

The parameters σ and ϵ , respectively, characterize the diameter of the atoms and the strength of their attractive interaction. Here, all thermodynamic states and properties will be presented in "Lennard-Jones units" such that $\sigma=1$ and $\epsilon/k_{\rm B}=1$, where $k_{\rm B}$ is Boltzmann's constant.

The equilibrium thermodynamic properties of the LJ model, including the equation of state, enthalpy, phase boundaries, critical point, and others, have been studied via molecular simulation by many researchers, and semi-empirical equations have been presented as convenient representations of these properties. The available fluid-phase data and fits have been thoroughly reviewed recently by Thol *et al.*, so we will not attempt to catalog them here. Simulation data and fits have also been presented for the LJ crystal ^{2–6} with attention recently given to the low-temperature hcp/fcc transition. ^{7–9}

In this paper, we focus on the crystal and low-temperature fluid phases, providing molecular simulation data for the

thermodynamic properties, from which we evaluate free energies and phase-coexistence conditions. We present data over the entire space of temperature and density where the crystal is stable, from zero temperature to the soft-sphere (SS) limit. We evaluate coexistence lines between the hcp and fcc crystals, between both crystals and the vapor and between the fcc crystal and the liquid. Recently developed simulation methods allow us to obtain results with very little stochastic error, which means that we have to give special attention to sources of systematic error in our data so that its accuracy is commensurate with the precision. We consider in particular finite-size effects, including truncation of the potential and extrapolation to the thermodynamic limit. We also account for the effects of vacancy defects on the free energy of the crystalline phases. On the other hand, all behavior is handled classically, and in particular, we do not include nuclear quantum effects (see Sec. II A 6).

The aims of this work are twofold: (1) to provide high-quality data and convenient empirical representations of it, which can be used to test theories and other simulation methods while quantifying the importance of often-neglected sources of inaccuracy, and (2) to demonstrate best practices for computing properties of simple crystals. In Sec. II, we describe the methods used and the formalism that compactly represents the thermodynamic space of temperature and density to encompass all crystal states. In Sec. III, we present and discuss the results of the calculations. We summarize and conclude in Sec. IV; a review of the key formulas representing the LJ properties is provided in this section, for the reader wishing to quickly access the primary results of this paper.

II. FORMALISM AND METHODS

The natural variables for specifying the thermodynamic state are the temperature T and number density ρ (or pressure P). However, these variables are inconvenient for the present purpose. We aim to characterize the crystalline phase over its entire region of stability. At a high temperature and density, the LJ model approaches the system of soft r^{-12} repulsive spheres, for which the thermodynamic state can be fully specified by the single group, ¹⁰

$$Y \equiv \frac{T}{4\rho^4}. (2)$$

For the stable LJ solid, Y is always less than about 0.5, whereas T and ρ can together take on arbitrarily large values. Likewise, it is helpful to work with the molar volume $v = 1/\rho$ rather than the density—for the stable solid v ranges from 0 (soft-sphere limit) to about 1.0. At a low temperature, the r^{-6} attraction becomes important, but no simple scaling form emerges. Still, we find it helpful to work with v^2 rather than v as the independent variable as it yields a more regular behavior in the

In terms of these variables, the pressure P and molar thermodynamic energy u are given via derivatives of the molar free energy $a(Y, v^2)$ as follows:

$$\left(\frac{\partial \beta a}{\partial Y}\right)_{p^2} = -\frac{\beta u}{Y},\tag{3a}$$

$$\left(\frac{\partial \beta a}{\partial v^2}\right)_Y = \frac{1}{2v^2} (4\beta u - Z),\tag{3b}$$

where $Z = Pv/k_BT$ is the compressibility factor. Our approach is to evaluate $u(Y, v^2)$ and $Z(Y, v^2)$ via molecular simulation and use these data to obtain the free energy via thermodynamic integration according to Eq. (3).

A. Fcc and hcp crystals

The molar Helmholtz free energy for a perfect crystal of N atoms can be separated into lattice (lat), quasiharmonic (qh), and anharmonic (ah) components,

$$a(Y, v^2) = u^{\text{lat}}(v^2) + a^{\text{qh}}(Y, v^2) + a^{\text{ah}}(Y, v^2).$$
 (4)

Each component can be evaluated using a method best suited for it.

1. Lattice contribution

The molar interatomic energy of the perfect lattice, u^{lat} $\equiv U^{\text{lat}}/N$, is given analytically in v^2 for each crystal structure, ¹¹

$$\begin{split} u_{\rm fcc}^{\rm lat}(v^2) &= 6.065\ 940\ 098\ 272\ 290/v^4 \\ &- 14.453\ 921\ 043\ 744\ 47/v^2, \\ u_{\rm hcp}^{\rm lat}(v^2) &= 6.066\ 146\ 884\ 549\ 459/v^4 \end{split} \tag{5a}$$

 $-14.45489727784168/v^2$.

The coefficients are obtained from lattice sums converged to

machine precision, with no cutoff applied to the potential. The lattice contribution to the pressure is

$$P^{\text{lat}} = -\frac{du^{\text{lat}}}{dv}.$$
 (6)

(5b)

2. Quasiharmonic contribution

The classical quasiharmonic contribution a^{qh} is given

$$\beta a^{\text{qh}}(T, \rho; r_c, N) = \frac{1}{2N} \sum_{i=1}^{3(N-1)} \ln \left(\frac{\lambda_i(\rho; N, r_c)}{2\pi k_B T} \right) - \frac{3}{2N} \ln N + \frac{1}{N} \ln \rho + 3 \ln \Lambda, \quad (7)$$

where the harmonic spring constants λ_i are obtained as described below and Λ is the thermal de Broglie wavelength, taken to be 1. These spring constants are, as indicated, dependent on N and the potential truncation distance r_c . For a given N, we isolate the contribution from the spring constants, $\sum \ln \lambda_i$, and evaluate this sum for several values of r_c , and these are extrapolated to $1/r_c \rightarrow 0$. This is repeated for increasing values of N, and the set of extrapolated results is again extrapolated to $1/N \rightarrow 0$. Thus, we evaluate the molar quasiharmonic free-energy contribution in the thermodynamic limit,

$$\beta a_{\infty}^{\text{qh}}(T,\rho) = -\frac{3}{2} \ln(2\pi k_B T) + \frac{1}{2N} \lim_{N,r_c \to \infty} \times \sum_{i}^{3(N-1)} \ln \lambda_i(\rho; N, r_c).$$
 (8)

The spring constants are obtained as eigenvalues of the dynamical matrix, 12,13 which yield λ_i . In principle, this involves construction of a $3N \times 3N$ Hessian matrix, with elements given by second derivatives of the potential with respect to each of the x, y, z coordinates of each atom. For large N, as needed for the limit in (8), this calculation is prohibitive. Instead, the symmetry of the lattice permits this process to be separated into many smaller pieces, each involving only nbasis atoms. 13 We construct a $3n \times 3n$ dynamical matrix **D** as a function of wave vector \mathbf{k} ,

$$\mathbf{D}(\mathbf{k}) = \sum_{\substack{\text{unit cells, } l'\\ r_{jj'} < r_c}} \mathbf{\Phi}(l') \exp(i\mathbf{k} \cdot \mathbf{R}(l')). \tag{9}$$

Here, $\mathbf{R}(l')$ is the coordinate of the origin of unit cell l', and the sum is over all unit cells having atoms within the cutoff r_c relative to atoms in the central cell. Each element of the force-constant matrix Φ pertains to the α coordinate (x, y, z)of basis-atom j in the central unit cell (l = 0) as it interacts with basis-atom j' in unit cell l', varying its α' coordinate. 13

For the fcc crystal, n = 4 and we select **k** as the reciprocal vectors for a cubic lattice,

$$\mathbf{k} = (k_1/K_1, k_2/K_2, k_3/K_3)2\pi/a,$$

$$k_i = -\lfloor (K_i - 1)/2 \rfloor \dots, \lfloor K_i/2 \rfloor;$$
(10)

the lattice constant is $a = (4v)^{1/3}$ and K_i is the number of cells in direction i; for fcc, this is the same in all directions and equal to $(N/4)^{1/3}$. For hcp, n = 4 and **k** are the reciprocal vectors for a rectangular lattice.

$$\mathbf{k} = (k_1/(K_1a), k_2/(K_23^{1/3}a), k_3/(K_3c))2\pi, \tag{11}$$

where nominally $c = (8/3)^{1/2}a$, but the exact proportion c/a is determined as described in Sec. II A 4. Also, we used $K_1 = 2K_2 = 2K_3 = N^{1/3}$.

Note that N has no relation to r_c in the framework, meaning that r_c can be larger than the box that would contain N atoms at density 1/v. Rather, N is just a convenient means to specify the number of wave vectors used for the analysis [facilitating the limit in (8)], while r_c describes the range for the lattice sum in (9). $\mathbf{D}(\mathbf{k})$ yields 3n eigenvalues (spring constants, λ_i) for each \mathbf{k} , and there are N/n \mathbf{k} -vectors for a given N, yielding 3(N-1) spring constants appearing in Eq. (7) plus 3 modes corresponding to center-of-mass motion.

With the formulas outlined above, we can obtain the lattice and quasiharmonic contributions to the classical free energy essentially exactly for the infinite system with no truncation of the potential. Having obtained the harmonic free energy for both finite-sized systems and the thermodynamic limit, we fit $\frac{1}{2N} \sum \ln \lambda_i$ as a function of density [see Ref. 14, Eq. (A3)],

$$\frac{1}{2N} \sum \ln \lambda_i = \frac{1}{N} \ln N + 7 \frac{N-1}{N} \ln \rho + \sum_i c_j v^{2j}, \quad (12)$$

where c_i are the fitting constants.

3. Anharmonic contribution

The anharmonic contribution is treated by fitting all simulation data—results for all temperatures, densities, and system sizes—to the functional form

$$\beta a^{\text{ah}}(Y, v^2; N) = \sum_{i=1}^{m_1} \sum_{j=0}^{m_1-i} c_{ij} Y^i v^{2j};$$
 (13)

this enforces the requirement that $\beta a^{\rm ah}$ vanish for $Y \to 0$ for all v^2 . To extrapolate to $N \to \infty$, we fit data for all system sizes to the form

$$\beta a^{\text{ah}}(Y, v^2) = \sum_{i=1}^{m_1} \sum_{j=0}^{m_1-i} c_{ij} Y^i v^{2j} + \frac{1}{N} \sum_{i=1}^{m_2} \sum_{j=0}^{m_2-i} d_{ij} Y^i v^{2j}$$
 (14)

and then evaluate the function with $N \to \infty$ (dropping the d_{ij} terms).

According to Eq. (3), the fitted quantities are

$$\theta^{Y} \equiv \left(\frac{\partial \beta a^{\text{ah}}}{\partial Y}\right)_{n^{2}} = -\frac{\beta u^{\text{ah}}}{Y},$$
 (15a)

$$\theta^{v^2} \equiv \left(\frac{\partial \beta a^{\text{ah}}}{\partial v^2}\right)_{V} = \frac{1}{2v^2} \left(4\beta u^{\text{ah}} - Z^{\text{ah}}\right); \tag{15b}$$

here we introduce θ^Y and θ^{v^2} as convenient representations of these derivatives. To perform the fit, simulation data for u^{ah} and Z^{ah} are used to compute θ^Y and θ^{v^2} for each simulated state point, and these are regressed to (13), appropriately differentiated according to (15). We note that θ^Y , which goes as u^{ah}/T^2 , is finite for $T \to 0$, 15 which is consistent with the

 $Y \to 0$ behavior of the fitting form. The upper limits of the sums in Eq. (13) are specified by m_1 and m_2 , which are chosen according to a χ^2 measure so as to neither over- nor under-fit the data. The objective function that is minimized to determine all c_{ij} and d_{ij} is

$$\Omega = \sum_{k} \frac{(\theta_{k}^{Y} - \theta_{\text{fit}}^{Y})^{2}}{\sigma_{\theta_{k}^{Y}}^{2}} + \frac{(\theta_{k}^{v^{2}} - \theta_{\text{fit}}^{v^{2}})^{2}}{\sigma_{\theta_{k}^{v^{2}}}^{2}} - \frac{2\rho_{\theta_{k}^{Y},\theta_{k}^{v^{2}}}(\theta_{k}^{Y} - \theta_{\text{fit}}^{Y})(\theta_{k}^{v^{2}} - \theta_{\text{fit}}^{v^{2}})}{\sigma_{\theta_{k}^{Y}}\sigma_{\theta_{v}^{v^{2}}}},$$
(16)

where $\rho_{\theta_k^Y,\theta_k^{v^2}}$ is the correlation between measured θ^Y and θ^{v^2} in simulation k

We evaluate the anharmonic contributions from molecular simulation using the recently introduced "harmonically mapped averaging" (HMA) formulas, ^{16,17} as given here,

$$\beta u^{\text{ah}} = \left\langle \beta u + \frac{1}{2N} \beta \mathbf{F} \cdot \Delta \mathbf{r} \right\rangle, \tag{17a}$$

$$Z^{\text{ah}} = \beta P^{\text{qh}} v + \frac{\beta}{3(N-1)} \left\langle \mathbf{F} \cdot \mathbf{r} + (\beta P^{\text{qh}} v - 1) \mathbf{F} \cdot \Delta \mathbf{r} \right\rangle, \tag{17b}$$

where u is the molar configurational energy for atoms in configuration \mathbf{r} (a vector of length 3N), \mathbf{F} is the corresponding vector representing the forces on all atoms, and $\Delta \mathbf{r}$ is the vector describing the displacements of all atoms from their associated lattice sites (hence, $\mathbf{F} \cdot \Delta \mathbf{r}$ and $\mathbf{F} \cdot \mathbf{r}$ are the sums of 3N terms). The angle brackets represent ensemble averages as taken in a molecular simulation using any conventional sampling method. Also, P^{qh} is the quasiharmonic estimate of the pressure obtained by differentiating the quasiharmonic free energy for the simulated system size [as given by (7) and (12)] with respect to volume.

The HMA formulas yield the anharmonic contributions to the properties directly. This contrasts with a more obvious approach that evaluates anharmonic behavior by subtracting the harmonic contributions from simulation averages taken using conventional methods. Consequently, the precision of the HMA results is tremendously enhanced because fluctuations associated with the harmonic behavior are not present. Separate treatment of the anharmonic behavior is advantageous with respect to accuracy as well, 15,16 as these contributions are in particular much less sensitive to finite-size effects in comparison with the harmonic contributions.

Special measures are used to evaluate behavior at very high temperatures, corresponding to the soft-sphere limit. This regime is obtained at $v^2 \to 0$ for finite (non-zero) Y. Here, θ^{v^2} remains finite even though its definition involves division by v^2 [cf. Eq. (15b)] because for the $4r^{-12}$ soft-sphere (SS) model $4\beta u = Z$ and the numerator is zero as well. We can collect data in this limit by simulating the soft-sphere system at an arbitrary density (we use $\rho = 1$) while varying T to examine a range of values of Y (which is the only variable needed to specify the SS thermodynamic state). Then, in place of Eq. (17), we evaluate averages according to [again, these yield results for $v^2 = 0$ to use in Eq. (15b)]

$$\frac{\beta u_{6}^{\text{ah}}}{v^{2}} = \left\langle \beta u_{\text{LJ}} + \frac{1}{2} \beta \mathbf{F}_{\text{LJ}} \cdot \Delta \mathbf{r} \right\rangle_{\text{SS}},$$

$$\frac{Z_{6}^{\text{ah}}}{v^{2}} = \beta v \left\langle \frac{1}{3V} \mathbf{F}_{\text{LJ}} \cdot \mathbf{r} + \left(-1/V + \beta P_{\text{SS}}^{\text{qh}} \right) \mathbf{F}_{\text{LJ}} \cdot \Delta \mathbf{r} \right.$$

$$+ \beta P_{\text{LJ6}}^{\text{qh}} \mathbf{F}_{\text{SS}} \cdot \Delta \mathbf{r} - P_{\text{LJ}}^{\text{lat}} \right\rangle_{\text{SS}}, \tag{18}$$

where the "LJ" subscript emphasizes that the quantity is evaluated for the full LJ potential (not SS), the subscript on the angle brackets indicates that sampling is performed based on the SS potential, and $P_{\rm LJ6}$ is the first-order correction to the quasiharmonic pressure in the limit of high density. Using (12), $\beta P_{\rm LJ6}^{\rm qh} = -2c_1$.

4. hcp lattice parameters

For the hcp phase, the equilibrium ratio of lattice constants, c/a, can vary from the ideal value $(8/3)^{1/2}$, in a manner depending on the temperature and density. To account for this effect, we have computed lattice, harmonic, and anharmonic contributions to the free energy due to variation of c/a from the ideal value. Because these deviations are very small, we can express the free energy change with a 2nd-order Taylor series 11,18 in terms of $\alpha \equiv (c/a)(3/8)^{1/2}$. The equilibrium α is then

$$\alpha^{\text{eq}} = -\left(\frac{\partial a}{\partial \alpha}\right) / \left(\frac{\partial^2 a}{\partial \alpha^2}\right),$$
 (19a)

and the free energy change is

$$a(\alpha^{\text{eq}}) = a(\alpha = 1) - \left(\frac{\partial a}{\partial \alpha}\right)^2 / \left(2\frac{\partial^2 a}{\partial \alpha^2}\right).$$
 (19b)

To evaluate these derivatives, the hcp lattice-energy constants appearing in (5b) were fit to values computed from $\alpha = 0.999$ to $\alpha = 1.001$ using a cubic polynomial in $\alpha - 1$. For the harmonic contribution, the form given in (12) is extended to a 2-dimensional fit,

$$\frac{1}{2N} \sum \ln \lambda_i = \frac{1}{N} \ln N + 7 \frac{N-1}{N} \ln \rho + \sum_{j,k} c_{jk} v^{2j} (\alpha - 1)^k.$$
(20)

Finally, the first derivative is computed by

$$\frac{\partial a}{\partial \alpha} = -\frac{2v}{3} \left(P_{zz} - (P_{xx} + P_{yy})/2 \right) \tag{21}$$

during *NVT* simulations conducted on the system with ideal geometry $\alpha = 1$ with the pressure components computed via standard formulas (without harmonically mapped averaging).

The anharmonic derivative is obtained by subtracting the lattice and harmonic free energy contributions and then correlating the values as a function of v^2 and Y with the form

$$\beta \frac{\partial a^{\text{ah}}}{\partial \alpha}(v^2, T) = \sum_{i=0}^{m} \sum_{j=0}^{m-i} c_{ij} Y^{i+1} v^{2j}.$$
 (22)

We assume that the anharmonic contribution to the 2nd derivative in (19) is zero. This assumption is supported by simulations conducted with $\alpha = 1.001$ which showed no statistical difference in the first derivative from $\alpha = 1$.

5. Vacancy-defect contribution

Lattice vacancies are a thermodynamically stable defect and will be present in some concentration in the equilibrium crystal. These vacancies have a significant effect on the free energy relative to the precision and accuracy of our calculations, so we need to account for them. Evaluation of vacancy concentration is complicated by the need to allow for equilibration with respect to an order parameter, described as the number of lattice sites, M. For a perfect crystal, N = M, but the system in principle is free to trade off (at fixed V, N) from this case to the one having more, smaller cells (hence different M), some of which are vacant. There is an entropic contribution gained in the form of a mixing entropy (i.e., a mixture of vacant and filled sites) that competes with the loss of entropy (or increase in energy) as the atoms are confined to smaller cells. Any simulation of feasible size using periodic boundary conditions finds it difficult if not impossible to sample M appropriately.

We circumvent this problem by working within the grand-canonical ensemble, fixing M and solving for the chemical potential that has the chosen M as its equilibrium value. Details are given in Ref. 20 and are rather lengthy, so we will not attempt to reproduce them here. The key output from the calculations is the equilibrium vacancy fraction $\phi = (M - N)/M$, and the difference in molar Helmholtz free energy between the vacancy-equilibrated crystal and the perfect lattice $\Delta a^{\text{vac}} \equiv a(\phi) - a(\phi = 0)$.

6. (Neglect of) nuclear quantum effects

Given that we consider temperatures extending as low as T=0, if attempting application to a real system with atoms of finite mass, m, nuclear quantum effects would be significant at some of the conditions examined in this study. It is a simple matter to accommodate these effects in u^{lat} and a^{qh} , as the non-classical forms are given analytically. To include nuclear quantum effects in a^{ah} , we would need to conduct simulations using a (T- and m-dependent) semiclassical form of the LJ potential or, for very low T and/or m, apply pathintegral methods. In principle, corresponding measures would also need to be applied for the gas and fluid phases. Presently we have no particular material (m) in mind, and we do not wish to do a parametric study of m, so we restrict our focus to purely classical behavior.

B. Gas phase

The gas phase pressure can be determined accurately using the virial equation of state, which expresses the compressibility factor Z as a series in the density^{21–23}

$$Z = 1 + B_2(T)\rho + B_3(T)\rho^2 + B_4(T)\rho^3 \dots$$
 (23)

An expression for the molar Helmholtz free energy can be derived from this,

$$\beta a(T, \rho) = 3 \ln \Lambda + \ln \rho - 1 + B_2(T)\rho + \frac{1}{2}B_3(T)\rho^2 + \dots$$
(24)

 B_n are the virial coefficients, which may be determined rigorously via numerical calculation for a given molecular model.

For the conditions of interest to this work, where the gas is in equilibrium with the crystalline solid, the density is very low; hence, the series is not required to high order. Values of coefficients are available²⁴ to sufficiently high order and with sufficient precision to allow us to compute the pressure and free energy with at least eight digits of accuracy and precision.

C. Liquid phase

We evaluate the free energy of the liquid phase using the form

$$\beta a^{\text{liq}}(Y, v^2) = \ln \rho - 1 + \sum_{i=0}^{m} \sum_{j=0}^{m-i} c_{ij} Y^{-i} v^{2j}$$
 (25)

with c_{00} set to match the soft-sphere fluid residual free energy at $Y = 1.8^{-1}$.

$$c_{00} = \beta A_{SS}(Y = 1.8^{-1}) - \ln \rho + 1 - \sum_{i=1}^{m} c_{i0} 1.8^{-i}.$$
 (26)

The soft-sphere fluid reference is well described by the virial equation of state, 25,26 for which coefficients up to the tenth order (B_{10}) are known. 25,27 Additionally, coefficients up to B_{13} were fit to *NVT* simulation data.

D. Computational details

1. Fluid phase

We conducted simulations for v^2 from 0 (soft-sphere limit) to 1.8, in a cubic box with periodic images. For each volume, we considered values of Y [Eq. (2)] in steps of 0.1 starting from a value slightly above the fcc-fluid coexistence point down to a value that is 0.8 less than it. We sampled configurations using a hybrid MD/Monte Carlo (MC) algorithm:²⁸ the atoms are propagated according to velocity Verlet MD²⁹ for segments of 20 time steps, each of size $\Delta t = \rho/125T^{1/2}$; at the end of each segment, the whole set of time steps are accepted or rejected via the Metropolis Monte Carlo algorithm, using the energies at the beginning and end of the MD segment. We found an acceptance rate of 91%-97%, depending on the system size. Sampling was performed using a force-shifted potential truncated at $r_c/v^{1/3}$ = 2.5, and averages were evaluated by reweighting to $r_c/v^{1/3}$ = 2.5 · 1.2 i with i ranging from 1 to 6 $(r_c/v^{1/3} \approx 7.5 \text{ for } i = 6)$. For cutoffs more than 0.494 of the box length, interactions were computed with a lattice sum of periodic images. For each truncation, the standard long-range correction was included for all properties. ²⁸ We examined system sizes N from 250 to 4000 atoms, with 1×10^6 MD time steps for each N at each state point.

Simulations for soft spheres [with $u^{(2)}(r) = 4r^{-12}$] were conducted at T = 1 and $N = 16\,000$ with densities ranging from 0.30 to 0.88 in increments of 0.01 (corresponding to Y from about 0.4 to 30.9). All simulations were performed for 10^6 steps using the same hybrid MD/MC strategy as used for the liquid simulations. Because truncation effects for soft spheres are much less severe than for Lennard-Jones, we considered reduced truncations up to only $2.5 \cdot 1.2^3 = 4.32$.

2. Fcc and hcp crystal phases

Simulations were performed for a grid of values of Y and v^2 encompassing the fcc and hcp crystalline phases, as estimated from previous studies in the literature. The points are displayed in Fig. 1. At each state, MC simulations were run for N=500 atoms, sampling 1×10^8 MC steps, up to N=4000, sampling 1×10^9 steps for the fcc phase. For hcp, simulations were performed for N=512 atoms, sampling 1×10^8 MC steps, up to N=4096, sampling 1×10^9 steps. Averages were recorded according to Eqs. (17) and (for hcp) (21).

E. Truncation of the potential

When considered on the scale of the accuracy and precision targeted in this work, truncation of the potential has a significant influence on the results, even when standard corrections are applied. For the crystal, the truncation is based on the distance between lattice sites, so atom pairs are defined to interact (or not) at the beginning of the simulation; the movement of the atoms in or out of the truncation during the simulation has no effect on whether they interact. The fluctuations in and out of the truncation radius are anharmonic (since they are not accounted for in the harmonic system) and persist to very low temperatures, so handling the truncation as we do allows us to collect anharmonic contributions with much better precision. For the fluid, the truncation radius is applied in the usual way: atom pairs interact when they are inside in the radius and stop interacting if they move away.

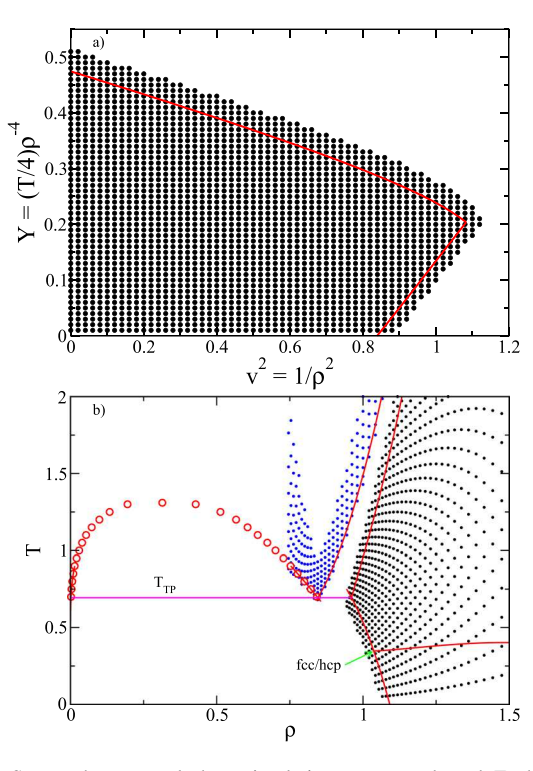


FIG. 1. States where crystal-phase simulations were conducted. Each black circle represents an independent simulation, while in (b), each blue circle represents a liquid simulation. Red lines show conditions of melting/sublimation and a tie line is drawn at the triple point. Open circles are vapor-liquid coexistence points from Ref. 30.

The truncation radius r_c is limited by the computational expense required to compute all the pair interactions, which of course grows with the cube of the radius. To handle this, we employ an approach in which a modest reduced truncation distance $r_{c,1}/v^{1/3} = 3$ is employed for sampling configurations. Data are collected every 2N steps at reduced truncation radii $(r_{c,2}/v^{1/3})$ of 3.0 and 3.5 (and 4.0 for $N \ge 864$).

We recover the desired larger- r_c properties from the $r_{c,1}$ -based samples through a reweighting formula. Specifically, we sample based on cutoff $r_{c,1}$ and evaluate a property W weighted for the (larger) cutoff $r_{c,2}$ as follows:

$$\langle W_2 \rangle_2 = \frac{\langle W_2 \exp[-\beta(U_2 - U_1)] \rangle_1}{\langle \exp[-\beta(U_2 - U_1)] \rangle_1},\tag{27}$$

where the 1 and 2 subscripts indicate a property evaluated according to interactions cut off at $r_{c,1}$ and $r_{c,2}$, respectively; likewise, the subscripts on the averages $\langle \dots \rangle$ indicate sampling with interactions U_1 or U_2 . We can observe the effect of r_c by evaluating the reweighted averages for several values of $r_{c,2}$ during a single simulation sampling according to $r_{c,1}$.

Additionally, we collect data every 10N steps using reduced truncation radii of 5.0, 6.0, 7.5, 9.0, and 11.0. These longer truncations require a lattice sum, especially for smaller systems. In order to prevent the increased data collection interval from increasing the uncertainty of the averages, we construct the final average as follows:

$$\langle W_3 \rangle_3 = \langle W_2 \rangle_2 + \left(\left\langle W_3^{LS} \right\rangle_3 - \left\langle W_2^{LS} \right\rangle_2 \right), \tag{28}$$

where each term is computed according to Eq. (27). The strong correlation between W_2^{LS} and W_3^{LS} yields a very small uncertainty for the difference.

The reweighted average given by Eq. (27) is biased, meaning that the expected value of $\langle W_2 \rangle_2$ differs from the correct value. An expression for this bias is derived in the Appendix, with the result

$$E[\langle W_2 \rangle_2] - \langle W_2 \rangle_2 = \frac{\langle W_2 \exp[-\beta(U_2 - U_1)] \rangle_1}{\langle \exp[-\beta(U_2 - U_1)] \rangle_1} \left(-\hat{\sigma}_{\text{ND}} + \hat{\sigma}_{\text{D}}^2 \right). \tag{29a}$$

From the propagation of error, the uncertainty is

$$\sigma_{\langle W_2 \rangle_2} = \frac{\langle W_2 \exp[-\beta (U_2 - U_1)] \rangle_1}{\langle \exp[-\beta (U_2 - U_1)] \rangle_1} (\hat{\sigma}_N^2 + \hat{\sigma}_D^2 - 2\hat{\sigma}_{ND})^{1/2}.$$
(29b)

In (29), $\hat{\sigma}_{N}^{2}$ and $\hat{\sigma}_{D}^{2}$ are the variances of the mean (squared uncertainties) for the numerator and denominator of (27), respectively, and $\hat{\sigma}_{ND}$ is the covariance of the two means; the caret on each σ indicates that these deviations are divided by their respective averages.

All of the error terms in (29) are made smaller by increasing the amount of sampling used for the average in (27). Because of the square root on the error in (29b), the uncertainty in $\langle W_2 \rangle_2$ will exceed its bias if sufficient sampling is performed, and hence we normally may neglect the bias. However in the present application, where we are combining many independent simulation results to obtain a single fitted

form, we must be more careful. Many of the simulations are likely to be biased in the same way such that the bias would remain intact after fitting even though the uncertainty might be substantially reduced. Accordingly, we have computed the bias and uncertainty using (29a) and (29b) and find that the bias in $(\partial \beta a^{ah}/\partial v^2)_Y$ never exceeds 7% of the uncertainty, while the bias in $(\partial \beta a^{ah}/\partial Y)_{v^2}$ never exceeds 4% of the uncertainty.

There is also potential for bias of the type known to sometimes afflict free-energy perturbation calculations. 31,32 This would result from inadequate sampling of configurations important to the $r_{c,2}$ system when sampling according to $r_{c,1}$. Given the nature of the perturbation, this is expected to be negligible.

III. RESULTS AND DISCUSSION

In this section, we present data computed using the methods outlined above and evaluate coexistence lines between the phases of interest. Fitting constants for the semi-empirical formulas appearing in Sec. II are reported in the supplementary material.

A. Finite-size effects

The limiting process used to evaluate $\beta a_{\infty}^{\rm qh}$ is shown in Figs. 2 and 3. Dependency of $\beta a^{\rm qh}$ on the potential cutoff r_c for fixed N is through the real-space sum for Φ in Eq. (9). Convergence with respect to the potential cutoff r_c is demonstrated in Fig. 2. The neglected contribution from $r > r_c$ decays as r_c^{-5} , so we plot the harmonic free energy against r_c^{-5} to obtain a nearly linear form that can be extrapolated to zero to obtain the infinite- r_c value. This process is performed for several values of N (i.e., the number of \mathbf{k} vectors in the reciprocal-space sum), each yielding an r_c -extrapolated value for a^{qh} . These values are plotted against 1/N and themselves extrapolated to $1/N \rightarrow 0$ to yield the infinite-system infinite-cutoff result for the quasiharmonic contribution to the free energy. The extrapolation is shown in Fig. 3. We subtract $N \ln N$ while doing the extrapolation because this is known to yield a more linear form.³³ We fit the resulting data with the function

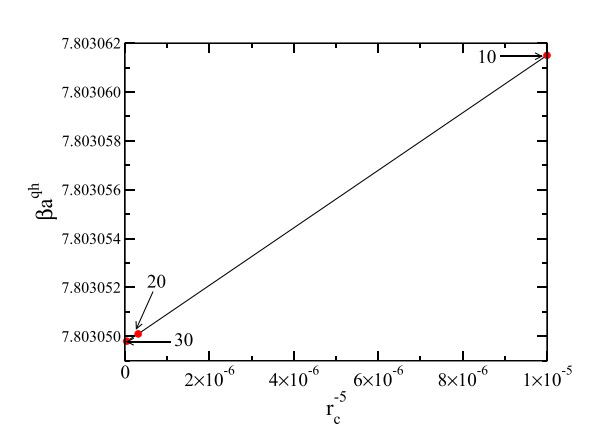


FIG. 2. Constructions showing extrapolation of the quasiharmonic contribution to the free energy with r_c . Data are for N = 186624.

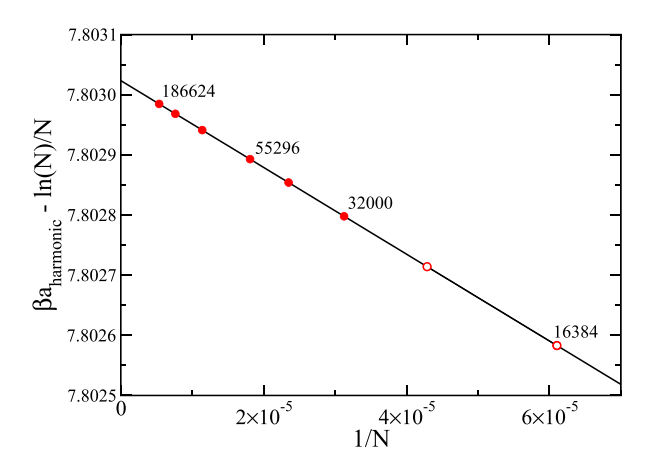


FIG. 3. Constructions showing extrapolation of the quasiharmonic contribution to the free energy. Labels on some of the points indicate the value of N. Open symbols at the two smallest system sizes were excluded from the fit because they could not be fit sufficiently well with a quadratic form.

$$\beta a^{\text{qh}} - \ln(N)/N = a_0 + a_1/N + a_2/N^2 + a_3 \ln(N)/N^2$$
. (30)

The effect of the potential truncation radius r_c and system size N on the anharmonic properties is demonstrated in Fig. 4. The variation with r_c is smoother than would be expected for the given error bars because the data for a single system size are highly correlated, inasmuch as they were all taken as averages for different $r_{c,2}$ using the same data as sampled according to $r_{c,1}$. The $r_c \to \infty$ limit is reached for r_c about 6, and the system size dependence is not significant in comparison with the uncertainties. This weak dependence of the anharmonic properties with N is consistent with observations made in previous work. 15,16,18

B. Properties

Results for the two derivatives θ^Y and θ^{v^2} defined in Eq. (15) are presented in Fig. 5 for the fcc crystal with N = 500. Data over the entire region of stability for the crystalline phase are presented, and it can be seen that all results are given to very high precision: the variation with Y is smooth, and although finely spaced in v^2 , the different isochores are easily discerned.

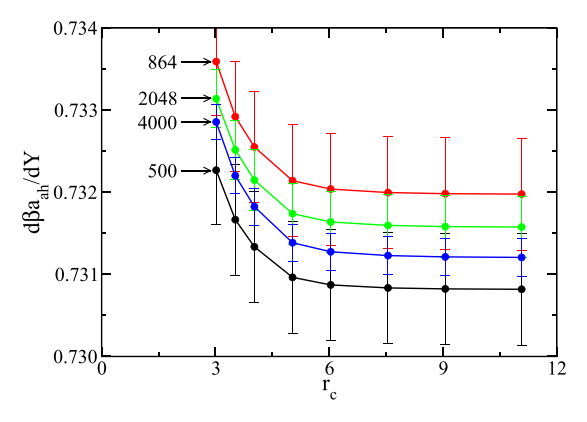


FIG. 4. Effect of truncation radius and system size on the *Y*-derivative of the anharmonic free energy. Error bars show 68% confidence limits. Conditions are $v^2 = 1.04$, Y = 0.24, corresponding to T = 0.89, $\rho = 0.98$.

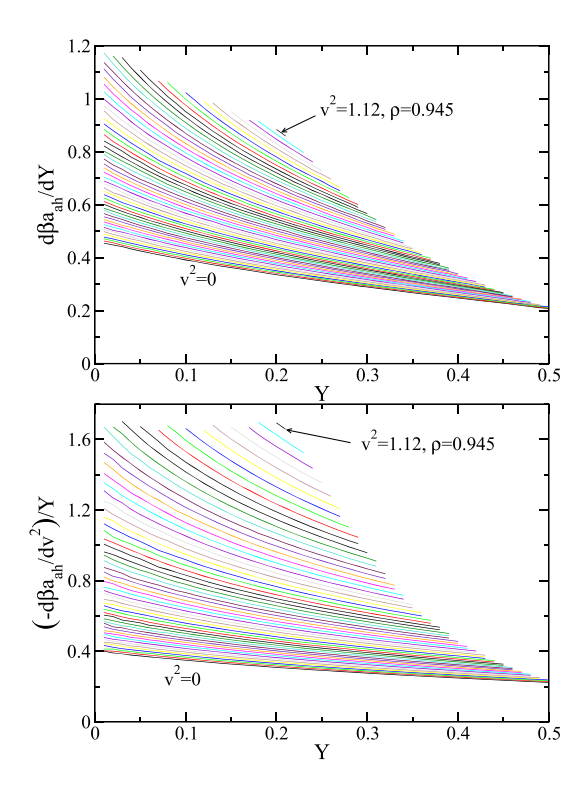


FIG. 5. Simulation results for the two anharmonic free energy derivatives given by Eq. (15). Data are for the N = 500 fcc crystal. Uncertainties (68% confidence) are smaller than the line thickness. Each line is an isochore, with values of v^2 that vary monotonically between the two indicated limits. Lines are colored differently to aid in distinguishing them.

The data are fit to the form defined via Eqs. (13), (15), and (16). The quality of the fit is demonstrated in Fig. 6, where the residuals in the fit of θ^Y to the N=500 data are presented. We see that there is no observable systematic deviation of the data from the fitting function. The θ^{v^2} fit performs equally well, and this figure is typical of other system sizes. When data for all N are fit according to Eq. (13), the sum of residuals gives a reduced χ^2 statistic of 1.05.

C. Vacancies

Detailed results for the vacancy concentration of the fcc crystal as a function of temperature and density have been

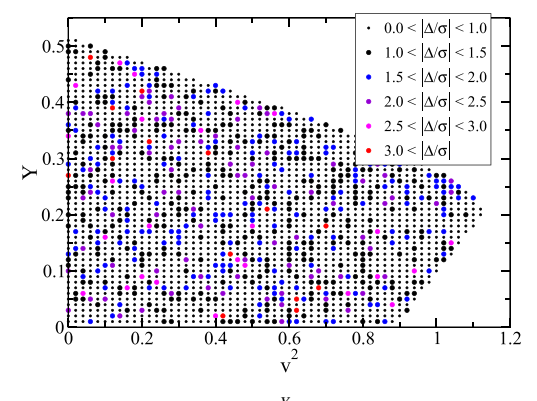


FIG. 6. Map of residuals for the fit of θ^Y to the form given by Eqs. (13)–(16). Each point shows $\Delta/\sigma_{\theta^Y} \equiv |\theta^Y_{\rm sim} - \theta^Y_{\rm fit}|/\sigma_{\theta^Y}$, where σ_{θ^Y} is the uncertainty in the simulation value, indicating the range it falls within, as defined in the legend.

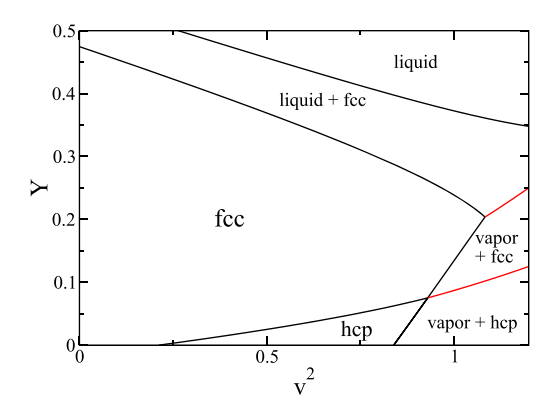


FIG. 7. Crystal-fluid coexistence diagram in the plane of $Y = Tv^4/4$ and v^2 . Red lines are triple lines (three-phase coexistence) for the phases in the adjacent two-phase regions. The hcp-fcc two-phase region is too small to see on the figure.

reported elsewhere.²⁰ In Tables S97–S99 of the supplementary material, we present fits of the fcc vacancy data that can be used in conjunction with the vacancy-free equation of state to predict the vacancy concentration, the effect on the free energy, and (through differentiation) other properties.

There have been recent reports^{6,34} of defects and disordering in crystals at temperatures below the melting point, dubbed "premelting" by researchers. While we find that vacancies are present near melting and have a small impact on properties, others have asserted that premelting is due to even higher-order defects such as line dislocations and that such defects can form spontaneously in defect-free systems. In the absence of defects we create (by removing an atom), we observe no net motion of any atom, which would occur if defects were forming spontaneously: the atoms simply vibrate about their lattice sites over the course of the simulations. We observe no qualitative difference between the properties near (or beyond) melting and properties at low temperatures. In particular, we see no anomalous behavior of the heat capacity, which has been suggested as an indicator of premelting.⁶ A more detailed comparison of properties we measured with those reported by Ref. 6 is included in the supplementary material.

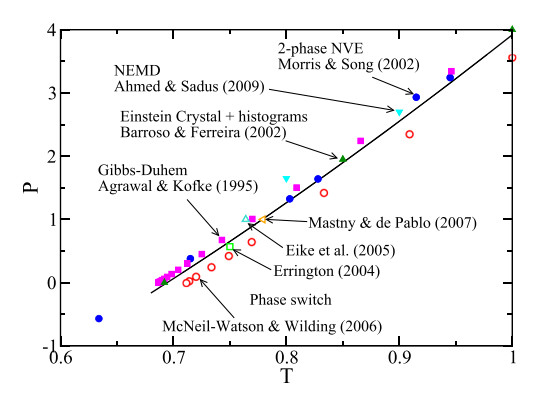


FIG. 8. Melting line in pressure-temperature plane. Literature data are results from direct coexistence simulations of Morris and Song, ³⁸ non-equilibrium dynamics simulations by Ahmed and Sadus, ³⁹ Einstein crystal and histogram reweighting simulations by Barroso and Ferreira, ³ Gibbs-Duhem integration by Agrawal and Kofke, ³⁶ and phase-switch methods by McNeil-Watson and Wilding, ⁴⁰ Errington, ⁴¹ Eike *et al.*, ⁴² and Mastny and de Pablo. ³⁷

D. Crystal-fluid coexistence lines

The full crystal-fluid phase diagram is shown in Fig. 7, including the line of coexistence between the hcp and fcc phases. Figure 8 presents the melting line in the more familiar pressure-temperature plane, where it is seen to be consistent with previously published results. Finite-size effects are not visible on the scale of this figure, so in Fig. 9, we expand the scale while plotting in reference to what should be our most accurate determination of this line. We present the results on several scales, to allow a fuller and more detailed comparison to previous calculations.

In the most expanded scale, it is possible to discern the effects of the finite size of the liquid phase. The difference between results for N = 2000 and N = 4000 is beyond their uncertainty estimates, but given that this difference is much reduced from the $N = 1000 \rightarrow 2000$ doubling, it is plausible that system-size inaccuracies in the N = 4000 results are less than their uncertainties.

Likewise, in Fig. 10, we demonstrate the effect on melting of the system size of the fcc crystal. Unlike for the liquid, the behavior is monotonic with N, and it is clear that the infinite-system behavior is represented well. We show also in this figure

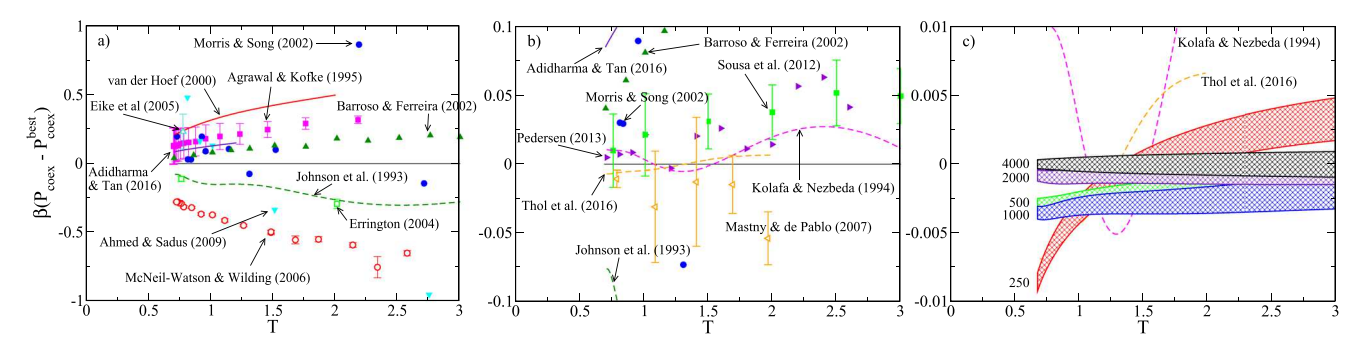


FIG. 9. Melting line in pressure-temperature plane, differenced with respect to our best estimate for this line to allow for an expanded scale. The "best" system used for this difference is based on the $N \to \infty$ fcc and the N = 4000 fluid-phase results. All plots present the same data but with a 10-fold expanding scale in each from left to right. Literature data are results from the work of Barroso and Ferreira, Morris and Song, 38 Agrawal and Kofke, 36 Errington, 41 McNeil-Watson and Wilding, 40 Adidharma and Tan, 9 Johnson *et al.*, 43 van der Hoef, 2 Thol *et al.*, 42 Pedersen, 44 Sousa *et al.*, 45 and Kolafa and Nezbeda. 46 The rightmost figure shows the effect of the simulation size (N) of the liquid phase, with the width of each shaded region representing its 68% confidence limits.

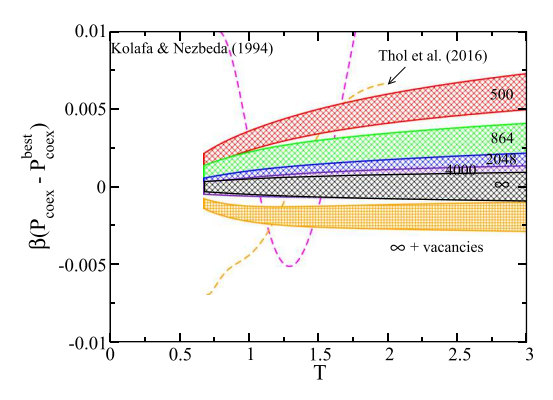


FIG. 10. Same as in Fig. 9(c) but showing the fcc-phase system-size effects in the calculation of the anharmonic contributions to the free energy and the effect of vacancies.

the effect of vacancies. The magnitude of the effect of vacancies on the melting pressure is comparable to that of simulating a crystal or fluid of size of order $N \approx 1000$. The shift in the coexistence line is represented well by the formula of Pronk and Frenkel.³⁵

$$P_{\rm melt}(\phi_{\rm eq}) - P_{\rm melt}(\phi = 1) = -\frac{\phi k_{\rm B}T}{v_{\rm liq} - v_{\rm fcc}}, \tag{31}$$

where ϕ is the vacancy fraction. Results for ϕ as a function of temperature and density are reported elsewhere.²⁰

Following previous studies, ^{2,4,36,37} we provide semiempirical representations of the melting line for the fcc-liquid coexistence and sublimation line for fcc-vapor coexistence in Table I

Finally, we note that to achieve accurate results it is not necessary to simulate the full grid of state points shown in Fig. 1. In the supplementary material, we present a revised determination of the fcc equation of state and coexistence with the liquid based on existing lattice and harmonic calculations

but replacing the anharmonic simulation data with data from 18 simulations of 256 atoms requiring less than 145 s of central processing unit (CPU) time. The resulting coexistence predictions are accurate but about 20 times less precise (comparable to the uncertainties in other simulation studies).

E. Fcc-liquid-vapor triple point

The intersection of the fcc-liquid and the fcc-vapor coexistence lines is the triple point, where fcc, liquid, and vapor all coexist. The conditions at the triple point are recorded in Table II, in comparison with the values reported previously in the literature. Results from our calculations are presented both with and without consideration of the effect of vacancy defects, and we see that their contribution is considerably larger than the uncertainty in the values. We have also used the equations of state for liquid and vapor to predict vapor-liquid equilibrium from the triple point to T=0.9 and report correlations for the coexistence properties in Table I. The predictions are almost consistent with calculations by Lotfi and co-workers, 30 but for the new results, the liquid density is about 10 times more precise and the pressure and vapor density are more than 100 times more precise.

F. Fcc-hcp coexistence line

Coexistence between the fcc and hcp crystals emerges at T=0 at a pressure P=878.5007 and continues to lower densities with increasing temperature, until it intersects the fcc-vapor coexistence line at $T=0.3474\pm0.0013$, forming a triple point; see Fig. 7. Properties at the endpoints of this coexistence line are summarized in Table III. These results are affected by deformation of the hcp lattice, and accordingly, we include coexistence results for both the ideal hcp lattice $(\alpha=1)$ and the one where the lattice is permitted to undergo

TABLE I. Correlations for coexistence properties of the Lennard-Jones model. All quantities in LJ units (such that $\sigma = 1$, $\epsilon/k_B = 1$). fcc-liquid correlations are valid for T > 0.68. Vapor-fcc correlations are valid for T > 0.75. fcc-hcp correlations are valid for $\rho > 1.368$. Vapor-liquid correlations are valid for 0.67 < T < 0.9.

#a	Property	Correlation ^b
1	Pliq/fcc	$\beta^{-5/4} \Big(16.50077 - 7.89468\beta^{1/2} - 3.80391\beta - 0.55658\beta^{3/2} - 0.96639\beta^2 + 1.38543\beta^{5/2} - 1.07794\beta^3 + 0.33176\beta^{7/2}\Big)$
2	$ ho_{ m melt}^{ m fcc}$	$\beta^{-1/2} \left(1.37785 - 0.40630\beta^{1/2} + 0.03069\beta - 0.00813\beta^{3/2} - 0.00460\beta^2 + 0.00082\beta^{5/2} - 0.00343\beta^3\right)^{-1/2}$
3	$ ho_{ ext{freeze}}^{ ext{liq}}$	$\beta^{-1/4} \Big(1.48202 - 0.37404 \beta^{1/2} + 0.05228 \beta + 0.05407 \beta^{3/2} - 0.20207 \beta^2 + 0.40137 \beta^{5/2} - 0.35589 \beta^3 + 0.12476 \beta^{7/2} \Big)^{-1/2}$
4	P ^{vap/fcc}	$\exp\left(\beta u_0^{\text{lat}} - \frac{1}{2}\ln T + 5.85227 - 0.35641T - 0.28917T^2 + 0.90556T^3 - 2.0684T^4 + 1.56928T^5\right)$
5	$ ho_{ m sub}^{ m fcc}$	$1.09151 - 0.14081T - 0.04152T^2 + 0.01828T^3 - 0.18547T^4 + 0.31686T^5 - 0.24139T^6$
6	$ ho_{ m dep}^{ m vap}$	$\exp\left(\beta u_0^{\text{lat}} - \frac{3}{2}\ln T + 5.85184 - 0.33797T - 0.51020T^2 + 1.97223T^3 - 4.30783T^4 + 3.28174T^5\right)$
7	Phcp/fcc	$47.71734 - 152.29990\rho + 199.61630\rho^2 - 157.42739\rho^3 + 42.52466\rho^4 + 18.29947\rho^5$
8	$ ho_{ m fcc/hcp}^{ m fcc}$	$\left(0.211819 + 12.41012Y - 34.871Y^2 - 14.59Y^3 - 1881.7Y^4 + 31778Y^5 - 151675Y^6\right)^{-1/2}$
9	$T^{hcp/fcc}$	$\Delta v^2/v^2 \left(0.322335 + 0.071798 \Delta v^2 + 0.055055 \Delta v^4 - 0.077536 \Delta v^6 + 0.385729 \Delta v^8 - 0.518442 \Delta v^{10} + 0.300867 \Delta v^{12}\right)$
10	$ ho^{ m hcp}$ – $ ho^{ m fcc}$	$-0.0087065 + 0.635861Y - 17.0213Y^2 + 448.668Y^3 - 7999.46Y^4 + 76730.4Y^5 - 314865Y^6$
11	$P^{\text{vap/liq}}$	$0.02300545 - 0.20899892T + 0.71851930T^2 - 1.15699885T^3 + 0.83711654T^4 - 0.18775604T^5$
12	$ ho_{ m cond}^{ m vap}$	$-0.07765874 + 0.48872094T - 1.19980513T^2 + 1.44918936T^3 - 0.91026263T^4 + 0.27923328T^5$
13	$ ho_{ m evap}^{ m liq}$	$4.5980714 - 21.3580461T + 50.3200157T^2 - 60.0837476T^3 + 35.7029650T^4 - 8.4772931T^5$

^a(1–3) freezing/melting, coexistence of fcc and liquid: (1) pressure; (2) fcc density; (3) liquid density; (4–6) sublimation, coexistence of fcc and vapor: (4) pressure; (5) fcc density; (6) vapor density; (7–10) polymorphism, hcp/fcc coexistence: (7) pressure; (8) fcc density; (9) temperature; (10) density change for fcc \rightarrow hcp transformation; (11–13) boiling/condensation, coexistence of liquid and vapor (valid for 0.69 < T < 0.9): (11) pressure; (12) vapor density; (13) liquid density.

^b $\beta = 1/T$; $Y = T/(4\rho^4)$; $u_0^{lat} = -8.610200156$; $\Delta v^{2n} = (v^2 - 0.211819)^n$.

TABLE II. Liquid-vapor-fcc triple-point properties for the Lennard-Jones model. All quantities in LJ units.

Source	T_{tp}	P_{tp}	$ ho_{ ext{tp}}^{ ext{liq}}$	$ ho_{ m tp}^{ m fcc}$
This work (with vacancies)	0.694 55(2) ^a	0.001 2637(5)	0.845 35(3)	0.960765(8)
This work (no vacancies)	0.69448(2)	0.001 2625(5)	0.845 37(2)	0.960813(6)
Heng et al. ⁴⁷	0.7085(5)	0.002 264(17)	0.8405(3)	0.9587(2)
Ahmed and Sadus ³⁹	0.661	0.0018	0.864	0.978
Mastny and de Pablo ³⁷	0.694			
Barroso and Ferreira ³	0.692	0.001	0.847	0.962
Chen et al. ⁴⁸	0.689(9)	0.001 29(22)	0.844(4)	0.955(5)
Agrawal and Kofke ³⁶	0.687(4)	0.0011	0.850	0.963
Ladd and Woodcock ⁴⁹	0.67(1)	-0.47(3)	0.818(4)	0.963(6)
Hansen and Verlet ⁵⁰	0.68(1)	•••	0.85(1)	

^aNumbers in parentheses indicate the 68% uncertainty in the rightmost digit(s) of the reported value.

homogeneous strain, adopting a value α^{eq} that minimizes the free energy according to Eq. (19).

Stillinger¹¹ reported T=0 hcp-fcc coexistence conditions based on converged lattice sums, just as we have done. Our results differ from his slightly due to additional precision that we have retained in our sums. We note that although the lattice sums give the energy to about 16 significant figures, the equilibrium T=0 pressure is given to about 11 figures. Stillinger discussed the effect of deformation of the hcp lattice and provided formulas that allow its effects to be computed but provided data only for the undeformed case (indicating that the deformation effect is small).

Travesset⁷ computed the harmonic free energy for fcc and hcp phases and determined coexistence between the two phases. He identified the triple point to be where the coexistence pressure was zero. The properties at the triple point are in reasonable agreement with values we computed using only harmonic contributions (also recorded in Table III) but showing slightly different densities—the difference in α is not sufficient to cause this, and instead it may be due to the less precise lattice energy used in Ref. 7 and the high sensitivity of the fcc-hcp coexistence curve to such inaccuracies. Calero *et al.*⁸ reported a vapor/hcp/fcc triple-point temperature that

differs substantially from ours. The source of this discrepancy is in the anharmonic contribution—according to Calero *et al.*, the anharmonic contributions strongly favor fcc, while we find that they weakly favor hcp. We do not otherwise have an explanation for this discrepancy.

Adidharma and Tan⁹ examined the properties of the fcc and hcp phases using molecular simulation, but their free-energy calculations used results from Calero *et al.*⁸ to determine a reference free-energy. Consequently their hcp-fcc coexistence line differs from ours as well, but this does not represent an independent comparison. Consistent with their specification of a lower triple-point temperature, their triple-point coexistence densities are higher than ours.

As seen in Fig. 7, the fcc-hcp coexistence curve is nearly a straight line in terms of v^2 and Y for the fcc phase even though the temperature behavior is more complex, going through a maximum of $T \approx 0.4028$. Accordingly, we provide correlations for the fcc-hcp coexistence curve in Table I in terms of Y, v^2 , and ρ , where each of these is the value for the fcc phase. The difference of the hcp density from the fcc density is smaller than the error in the fit but can be obtained from the correlation for $\rho^{\text{hcp}} - \rho^{\text{fcc}}$. At a low temperature (and high density), the fcc phase is more dense, while the hcp phase is more

TABLE III. Conditions at the endpoints of the hcp-fcc coexistence line for the Lennard-Jones model. All quantities in LJ units.

Source	$lpha^{ m a}$	T	P	$ ho^{ m fcc}$	$ ho^{ m hcp}$
This work	1.000 004 856	0	878.496 912 704	2.172 791 1923	2.172 782 464 35
This work	1	0	878.485 537 367	2.172 786 23477	2.172 777 506 17
Stillinger ¹¹	1	0	878.486 276 395	2.172 786 55676	2.172 777 828 26
Travesset ⁷	1	0	878.49	2.172 787 9	2.1727794
This work	0.999 812 76	0.347 4(13) ^b	$8.8(9) \times 10^{-9}$	1.036 8(2)	1.0368(2)
This work	1	0.347 0(13)	$8.6(8) \times 10^{-9}$	1.0369(2)	1.0369(2)
This work (harmonic)	0.999 892 57	0.319 183 8	0.9631×10^{-9}	1.038 5946	1.038 6084
Travesset ⁷ (harmonic)	1	0.319		1.038 8024	1.038 8161
Calero et al.8	1	0.13			
Adidharma and Tan9	1	0.13 ^c		1.072 515	1.072 518

^aThe reduced hcp c/a ratio α is unity for the ideal (undistorted) lattice.

^bNumbers in parentheses indicate the 68% uncertainty in the rightmost digit(s) of the reported value.

^cFit to match that in the work of Calero et al.⁸

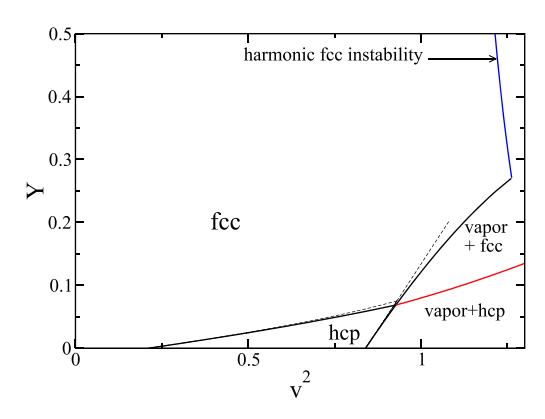


FIG. 11. Same as Fig. 7 but computed while excluding anharmonic contributions to properties (solid lines). The hcp-fcc-vapor triple line is in red. Dashed lines show behavior with full anharmonic contributions, for reference (these are the same as in Fig. 7).

dense at low pressure (near the fcc-hcp-vapor triple point). The density of the two phases is equal where the temperature is a maximum.

G. Importance of anharmonic effects on coexistence

Given the effort needed to account for anharmonic effects. it is of interest to examine what happens if we include only lattice and harmonic contributions to the properties of the crystal phases, neglecting anharmonic contributions entirely. Accordingly, Fig. 11 presents the phase diagram for the fcc crystal in the absence of anharmonic effects (cf. Fig. 7). The most striking outcome is the complete loss of the melting transition such that the harmonic fcc phase never loses stability with respect to the liquid, at any temperature; a description of this behavior in terms of the free energy is given in the supplementary material. The transition to the vapor (sublimation) remains and is shifted to lower temperatures. For higher temperatures, at sufficiently low density, the fcc crystal becomes mechanically unstable (dP/dv > 0); this instability continues to lower temperatures but is interrupted by the sublimation line, where the crystal becomes thermodynamically unstable with respect to the vapor.

The effect on the fcc/hcp coexistence is small, lowering the transition temperature slightly (see Table III)—anharmonic contributions favor the hcp phase.

IV. SUMMARY AND CONCLUSIONS

For the convenience of the reader, we provide here a summary of the formulas one should use to compute the infinite-system crystal properties reported here.

- Given a temperature T and density ρ of interest, compute $Y = T/4\rho^4$ and $v^2 = 1/\rho^2$. Note that all quantities are given in LJ units such that $\sigma = 1$, $\epsilon/k_{\rm B} = 1$.
- Molar free energy of fcc or undistorted hcp crystal. Evaluate according to the sum of terms in Eq. (4) (allowing N → ∞ where needed): u^{lat} is given by Eq. (5); a^{qh} is given by Eq. (8) with the sum over ln λ_i given by Eq. (12) (fcc, with constants c_j given in Table S10) or Eq. (20) (for hcp with α = 1, with c_{j,0} given in Table S15); a^{ah} is given by Eq. (13) with c_{ij} given in Table S20 for fcc and Table S55 for hcp. Note that this free energy is based on a unit value of the thermal de Broglie wavelength, Λ = 1.
- Thermodynamic properties of crystal. The five first and second derivatives of the free-energy with respect to T and v can be obtained from the formulas developed here. We summarize them in Table IV.
- *hcp distortion* fits for free energy derivatives with respect to α are provided in Tables S88–S90 of the supplementary material. These can be used with Eq. (19) to obtain the distortion and its effect on the free energy. An extended discussion of the distortion of the hcp phase is also presented in the supplementary material.
- Vacancy effects. Concentration of vacancy defects and their free-energy contribution are provided as fits in Tables S97–S99 of the supplementary material. The original simulation data are available in Ref. 20.
- Solid(fcc)-liquid coexistence (melting) line. Table I gives the coexistence pressure (#1) and densities (#2 and #3) as a function of temperature (via $\beta = 1/T$). This applies from the soft-sphere limit ($\beta \rightarrow 0$) to the fcc/liquid/vapor triple point, $\beta \approx 1.44$ ($T \approx 0.694$; Table II).
- Solid-vapor coexistence (sublimation) line. Table I gives the coexistence pressure (#4) and densities (#5

TABLE IV. Expressions for thermodynamic properties in terms of semi-empirical fits of free energy.

Property	Definition	Formula ^{a,b,c}
Internal energy	βи	$\beta u^{\text{lat}} + 1.5 - \sum_{i,j} i c_{ij} Y^i v^{2j}$
Pressure	eta P v	$\beta P^{\text{lat}}v + 7 - 2\sum_{j}jc_{j}v^{2j} - 2\sum_{i,j}(2i+j)c_{ij}Y^{i}v^{2j}$
Isochoric heat capacity	$\frac{c_v}{k_{\rm B}} = \frac{1}{k_{\rm B}} \left(\frac{\partial u}{\partial T} \right)_v$	$1.5 - \sum_{i,j} i(i+1)c_{ij}Y^iv^{2j}$
Isothermal bulk modulus	$\beta vB = -\beta v^2 \left(\frac{\partial P}{\partial v}\right)_T$	$\beta v^2 \frac{dP^{\text{lat}}}{dv} + 7 + 2 \sum_{j} j(2j-1)c_j v^{2j} + 2 \sum_{i,j} (2i+j)(4i+2j-1)c_{ij} Y^i v^{2j}$
Isochoric thermal pressure coefficient ^d	$\frac{v\gamma_{\rm v}}{k_{\rm B}} = \frac{v}{k_{\rm B}} \left(\frac{\partial P}{\partial T}\right)_v$	$7 - 2\sum_{j} jc_{j}v^{2j} - 2\sum_{i,j} (2i+j)(i+1)c_{ij}Y^{i}v^{2j}$

^aExpression for dimensionless quantity as given in the "definition" column. Also, $Y = Tv^4/4$.

^bLimits on the *i*, *j* double sums are $1 \le i \le m_1$, $0 \le j \le m_1 - i$.

culat is given by Eq. (5) and Plat is given by Eq. (6). Polynomial coefficients are given in the supplementary material: cj in Tables S10 and S15 and cij in Tables S20 and S55.

^d Volume expansivity is $\alpha_P \equiv (1/v)(\partial v/\partial T)_P = \gamma_v/B$.

and #6) as a function of T. This is valid from T = 0 to the fcc/liquid/vapor triple point $T \approx 0.694$ (Table II). The crystal form changes from hcp to fcc as T increases through the hcp/fcc/vapor triple point, $T \approx 0.347$ (Table III).

• hcp/fcc coexistence line. Coexistence properties are given in Table I, including the density of the fcc phase (#8) as a function of Y, the temperature (#9) as a function of v^2 , and the difference in density between hcp and fcc phases (#10) as a function of Y.

Although this study of the LJ crystal aimed to be comprehensive (at least with respect to conditions where the crystal is stable), inevitably there are some effects or behaviors of interest which have not been included here and which could be significantly relative to the accuracy and precision of our results. We discussed neglect of nuclear quantum effects in Sec. II A 6; one might also have interest in other types of defects apart from vacancies, such as stacking faults (interstitials are likely to be negligible). We have not computed elastic properties other than the bulk modulus, omitting consideration of shear moduli or related quantities. We have also not examined transport properties. Nevertheless, subsequent studies along these lines have a new standard of accuracy and precision to aim for in collecting properties. Moreover, new theoretical treatments and simulation methods should benefit from having a map of the properties with the precision and accuracy obtained here and convenient semi-empirical representations of the same.

SUPPLEMENTAL MATERIAL

See supplementary material for additional results and discussion as well as tables of raw data and coefficients of fits as described in this manuscript. Python codes that implement the equations described here are available upon request.

ACKNOWLEDGMENTS

This work is supported by the U.S. National Science Foundation through Grant No. OAC-1739145.

APPENDIX: DERIVATION OF EQ. (29a)

Any given simulation run will yield averages for the numerator and denominator of Eq. (27) that have a random error, $\hat{\epsilon}_N$ and $\hat{\epsilon}_D$, respectively, defined as fractions with respect to the true averages (indicated by the hat). Assuming that averaging is performed properly, the expected values of these errors are zero, $E[\hat{\epsilon}_N] = E[\hat{\epsilon}_D] = 0$, and moreover, their characteristic size (i.e., the uncertainty in their respective averages) diminishes inversely with the amount of sampling, $\hat{\sigma}_X^2 \equiv E(\hat{\epsilon}_X^2) \sim n_{\text{samp}}^{-1}, (n_{\text{samp}} \to \infty), X = \{\text{N,D}\}$. However, when subject to a non-linear transformation, such as in Eq. (27), these stochastic errors can introduce a systematic error in the transformed quantity. In particular, the expected value of the ratio is

$$E[\langle W_{2} \rangle_{2}] = E\left[\frac{\langle W_{2} \exp[-\beta(U_{2} - U_{1})] \rangle_{1}(1 + \hat{\epsilon}_{N})}{\langle \exp[-\beta(U_{2} - U_{1})] \rangle_{1}(1 + \hat{\epsilon}_{D})}\right]$$

$$= \frac{\langle W_{2} \exp[-\beta(U_{2} - U_{1})] \rangle_{1}}{\langle \exp[-\beta(U_{2} - U_{1})] \rangle_{1}}$$

$$\times E\left[(1 + \hat{\epsilon}_{N})(1 - \hat{\epsilon}_{D} + \hat{\epsilon}_{D}^{2} - O(\hat{\epsilon}_{D}^{3}))\right]$$

$$= \langle W_{2} \rangle_{2} \left(1 - E[\hat{\epsilon}_{N} \hat{\epsilon}_{D}] + E[\hat{\epsilon}_{D}^{2}]\right)$$

$$= \langle W_{2} \rangle_{2} \left(1 - \hat{\sigma}_{ND} + \hat{\sigma}_{D}^{2}\right). \tag{A1}$$

A simple rearrangement yields (29a).

- ¹M. Thol, G. Rutkai, A. Köster, R. Lustig, R. Span, and J. Vrabec, "Equation of state for the Lennard-Jones fluid," J. Phys. Chem. Ref. Data 45, 023101 (2016).
- ²M. A. van der Hoef, "Free energy of the Lennard-Jones solid," J. Chem. Phys. **113**, 8142 (2000).
- ³M. A. Barroso and A. L. Ferreira, "Solid-fluid coexistence of the Lennard-Jones system from absolute free energy calculations," J. Chem. Phys. 116, 7145 (2002).
- ⁴M. A. Van der Hoef, "Gas–solid coexistence of the Lennard-Jones system," J. Chem. Phys. **117**, 5092 (2002).
- ⁵D. M. Heyes and A. C. Brańka, "The Lennard-Jones melting line and isomorphism," J. Chem. Phys. **143**, 234504 (2015).
- ⁶A. Köster, P. Mausbach, and J. Vrabec, "Premelting, solid-fluid equilibria, and thermodynamic properties in the high density region based on the Lennard-Jones potential," J. Chem. Phys. **147**, 144502 (2017).
- ⁷A. Travesset, "Phase diagram of power law and Lennard-Jones systems: Crystal phases," J. Chem. Phys. **141**, 164501 (2014).
- ⁸C. Calero, C. Knorowski, and A. Travesset, "Determination of anharmonic free energy contributions: Low temperature phases of the Lennard-Jones system." J. Chem. Phys. **144**, 124102 (2016).
- ⁹H. Adidharma and S. P. Tan, "Accurate Monte Carlo simulations on FCC and HCP Lennard-Jones solids at very low temperatures and high reduced densities up to 1.30," J. Chem. Phys. **145**, 014503 (2016).
- ¹⁰W. G. Hoover, S. G. Gray, and K. W. Johnson, "Thermodynamic properties of the fluid and solid phases for inverse power potential," J. Chem. Phys. 55, 1128–1136 (1971).
- ¹¹F. H. Stillinger, "Lattice sums and their phase diagram implications for the classical Lennard-Jones model," J. Chem. Phys. 115, 5208–5212 (2001).
- ¹²M. Born and K. Huang, *Dynamical Theory of Crystal Lattices*, International Series of Monographs on Physics (Clarendon Press, 1954).
- ¹³ M. T. Dove, *Introduction to Lattice Dynamics* (Cambridge University Press, New York, 2005).
- ¹⁴T. B. Tan, A. J. Schultz, and D. A. Kofke, "Efficient calculation of temperature dependence of solid-phase free energies by overlap sampling coupled with harmonically targeted perturbation," J. Chem. Phys. 133, 134104 (2010)
- ¹⁵S. G. Moustafa, A. J. Schultz, and D. A. Kofke, "Harmonically assisted methods for computing the free energy of classical crystals by molecular simulation: A comparative study," J. Chem. Theory Comput. 13, 825–834 (2017).
- ¹⁶S. G. Moustafa, A. J. Schultz, and D. A. Kofke, "Very fast averaging of thermal properties of crystals by molecular simulation," Phys. Rev. E 92, 043303 (2015).
- ¹⁷ A. J. Schultz, S. G. Moustafa, W. Lin, S. J. Weinstein, and D. A. Kofke, "Reformulation of ensemble averages via coordinate mapping," J. Chem. Theory Comput. 12, 1491–1498 (2016).
- ¹⁸S. G. Moustafa, A. J. Schultz, E. Zurek, and D. A. Kofke, "Accurate and precise *ab initio* anharmonic free-energy calculations for metallic crystals: Application to hcp Fe at high temperature and pressure," Phys. Rev. B 96, 014117 (2017).
- ¹⁹W. Swope and H. Andersen, "Thermodynamics, statistical thermodynamics, and computer simulation of crystals with vacancies and interstitials," Phys. Rev. A 46, 4539–4548 (1992).
- ²⁰ A. Purohit, A. Schultz, S. Moustafa, J. Errington, and D. Kofke, "Free energy and concentration of crystalline vacancies by molecular simulation," Mol. Phys. 116, 3027 (2018).
- ²¹E. Mason and T. Spurling, *The Virial Equation of State* (Pergamon Press, Oxford, 1969).
- ²²J.-P. Hansen and I. McDonald, *Theory of Simple Liquids*, 3rd ed. (Academic Press, London, 2006).

- ²³ A. J. Masters, "Virial expansions," J. Phys.: Condens. Matter 20, 283102 (2008).
- ²⁴C. Feng, A. J. Schultz, V. Chaudhary, and D. A. Kofke, "Eighth to sixteenth virial coefficients of the Lennard-Jones model," J. Chem. Phys. **143**, 044504 (2015).
- ²⁵T. B. Tan, A. J. Schultz, and D. A. Kofke, "Virial coefficients, equation of state, and solid-fluid coexistence for the soft sphere model," Mol. Phys. 109, 123–132 (2011).
- ²⁶N. S. Barlow, A. J. Schultz, S. J. Weinstein, and D. A. Kofke, "An asymptotically consistent approximant method with application to soft- and hard-sphere fluids," J. Chem. Phys. **137**, 204102 (2012).
- ²⁷R. J. Wheatley, "Calculation of high-order virial coefficients with applications to hard and soft spheres," Phys. Rev. Lett. 110, 200601 (2013).
- ²⁸D. Frenkel and B. Smit, *Understanding Molecular Simulation: From Algorithms to Applications* (Academic Press, San Diego, 2002).
- ²⁹ M. P. Allen and D. J. Tildesley, *Computer Simulation of Liquids* (Oxford University Press, New York, 1987).
- ³⁰ A. Lotfi, J. Vrabec, and J. Fischer, "Vapour liquid equilibria of the Lennard-Jones fluid from the NpT plus test particle method," Mol. Phys. 76, 1319–1333 (1992).
- ³¹D. A. Kofke, "Getting the most from molecular simulation," Mol. Phys. 102, 405–420 (2004).
- ³²D. A. Kofke, "Free energy methods in molecular simulation," Fluid Phase Equilib. 228, 41–48 (2005).
- ³³W. G. Hoover, "Entropy for small classical crystals," J. Chem. Phys. 49, 1981–1982 (1968).
- ³⁴L. Gómoez, A. Dobry, C. Geuting, H. T. Diep, and L. Brukovsky, "Dislocation lines as the precursor of the melting of crystalline solids observed in Monte Carlo simulations," Phys. Rev. Lett. 90, 095701 (2003).
- ³⁵S. Pronk and D. Frenkel, "Point defects in hard-sphere crystals," J. Phys. Chem. B 105, 6722–6727 (2001).
- ³⁶R. Agrawal and D. A. Kofke, "Thermodynamic and structural properties of model systems at solid-fluid coexistence. II. Melting and sublimation of the Lennard-Jones system," Mol. Phys. 85, 43–59 (1995).
- ³⁷E. A. Mastny and J. J. de Pablo, "Melting line of the Lennard-Jones system, infinite size, and full potential," J. Chem. Phys. 127, 104504 (2007).

- ³⁸J. R. Morris and X. Song, "The melting lines of model systems calculated from coexistence simulations," J. Chem. Phys. 116, 9352–9358 (2002).
- ³⁹A. Ahmed and R. J. Sadus, "Solid-liquid equilibria and triple points of n-6 Lennard-Jones fluids," J. Chem. Phys. 131, 174504 (2009).
- ⁴⁰G. C. McNeil-Watson and N. B. Wilding, "Freezing line of the Lennard-Jones fluid: A phase switch Monte Carlo study," J. Chem. Phys. **124**, 064504 (2006).
- ⁴¹J. R. Errington, "Solid-liquid phase coexistence of the Lennard-Jones system through phase-switch Monte Carlo simulation," J. Chem. Phys. 120, 3130–3141 (2004).
- ⁴²D. M. Eike, J. F. Brennecke, and E. J. Maginn, "Toward a robust and general molecular simulation method for computing solid-liquid coexistence," J. Chem. Phys. **122**, 014115 (2005).
- ⁴³J. Johnson, J. Zollweg, and K. Gubbins, "The Lennard-Jones equation of state revisited," Mol. Phys. 78, 591–618 (1993).
- ⁴⁴U. R. Pedersen, "Direct calculation of the solid-liquid Gibbs free energy difference in a single equilibrium simulation," J. Chem. Phys. **139**, 104102 (2013).
- ⁴⁵J. M. G. Sousa, A. L. Ferreira, and M. A. Barroso, "Determination of the solid-fluid coexistence of the n 6 Lennard-Jones system from free energy calculations," J. Chem. Phys. **136**, 174502 (2012).
- ⁴⁶J. Kolafa and I. Nezbeda, "The Lennard-Jones fluid: An accurate analytic and theoretically-based equation of state," Fluid Phase Equilib. 100, 1–34 (1994).
- ⁴⁷V. R. Heng, M. Nayhouse, M. Crose, A. Tran, and G. Orkoulas, "Communication: Direct determination of triple-point coexistence through cell model simulation," J. Chem. Phys. **137**, 141101 (2012).
- ⁴⁸B. Chen, J. I. Siepmann, and M. L. Klein, "Direct Gibbs ensemble Monte Carlo simulations for solid-vapor phase equilibria: Applications to Lennard-Jonesium and carbon dioxide," J. Phys. Chem. B **105**, 9840–9848 (2001).
- ⁴⁹A. J. C. Ladd and L. V. Woodcock, "Interfacial and co-existence properties of the Lennard-Jones system at the triple point," Mol. Phys. 36, 611–619 (1978).
- ⁵⁰J.-P. Hansen and L. Verlet, "Phase transitions of the Lennard-Jones system," Phys. Rev. **184**, 151–161 (1969).